

Spin-valley coupling in single-electron bilayer graphene quantum dots

L. Banszerus,^{1,2,*} S. Möller,^{1,2,*} C. Steiner,^{1,2} E. Icking,^{1,2} S. Trellenkamp,³
F. Lentz,³ K. Watanabe,⁴ T. Taniguchi,⁵ C. Volk,^{1,2} and C. Stampfer^{1,2,†}

¹JARA-FIT and 2nd Institute of Physics, RWTH Aachen University, 52074 Aachen, Germany, EU

²Peter Grünberg Institute (PGI-9), Forschungszentrum Jülich, 52425 Jülich, Germany, EU

³Helmholtz Nano Facility, Forschungszentrum Jülich, 52425 Jülich, Germany, EU

⁴Research Center for Functional Materials, National Institute for Materials Science, 1-1 Namiki, Tsukuba 305-0044, Japan

⁵International Center for Materials Nanoarchitectonics,
National Institute for Materials Science, 1-1 Namiki, Tsukuba 305-0044, Japan

(Dated: December 23, 2024)

Understanding how the electron spin is coupled to orbital degrees of freedom, such as a valley degree of freedom in solid-state systems is central to applications in spin-based electronics and quantum computation. Recent developments in the preparation of electrostatically-confined quantum dots in gapped bilayer graphene (BLG) enables to study the low-energy single-electron spectra in BLG quantum dots, which is crucial for potential spin and spin-valley qubit operations. Here, we present the observation of the spin-valley coupling in a bilayer graphene quantum dot in the single-electron regime. By making use of a highly-tunable double quantum dot device we achieve an energy resolution allowing us to resolve the lifting of the fourfold spin and valley degeneracy by a Kane-Mele type spin-orbit coupling of $\approx 65 \mu\text{eV}$. Also, we find an upper limit of a potentially disorder-induced mixing of the K and K' states below $20 \mu\text{eV}$.

The valley pseudospin is an inherent property of two-dimensional honeycomb crystals and – together with the electron spin – makes graphene and bilayer graphene (BLG) interesting for applications in spin- and valley-based electronics and quantum computation [1, 2]. This pseudospin arises from the orbital degree of freedom of the independent energy valleys located at the inequivalent vertices (K and K') of the hexagonal Brillouin zone [3]. In analogy to the real spin, the valley pseudospin exhibits also a valley Zeeman effect [4–6], where the valley Zeeman splitting – varying linearly with (out-of-plane) magnetic field – is a result of the orbital magnetic moments originating from the non-vanishing Berry curvature, Ω , at the K -points of gapped BLG (see Fig. 1(a)). Since these magnetic moments, which have opposite signs for the two valleys, crucially depend on the wave function, the valley g -factor in BLG quantum dots can be tuned by electric fields [7, 8], offering promising and interesting possibilities for manipulation. However, to fully exploit the potential to manipulate and control both the valley and spin degrees of freedom in BLG quantum dots (QDs), a detailed understanding of their interaction is essential. This is as relevant for a better understanding of spin decoherence processes as it is for exploring ways to electrically manipulate the spin degree of freedom via spin-orbit interaction and implementing innovative spin-valley qubits [2]. Indeed, a detailed understanding of the low-energy spectrum of single particle states within the first electronic orbital (see Fig. 1(b)) is crucial for finding suitable working points and manipulation mechanisms for possible qubit operation.

Although the single-particle spectrum in BLG QDs has

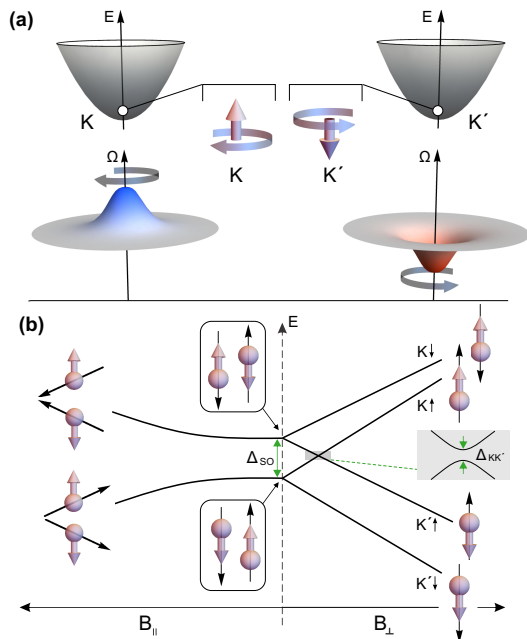


FIG. 1. (a) Low energy band schematic of BLG at the K and K' points. BLG exhibits a non-trivial Berry curvature Ω that leads to an effective out-of-plane magnetic moment with opposite sign at K and K' . (b) Energy dispersion of single-particle states in BLG QDs as a function of in-plane (B_{\parallel} , left) and out-of-plane (B_{\perp} , right) applied magnetic fields with respect to the BLG plane. The SO gap, Δ_{SO} , lifts the fourfold degeneracy and polarizes the spins out-of-plane for zero magnetic field and a potential K - K' state mixing (described by $\Delta_{\text{KK}'}$) leads to an anticrossing of the $K\uparrow$ and $K'\uparrow$ state.

* These two authors contributed equally.

† stampfer@physik.rwth-aachen.de

been intensively studied in recent years [9–11], the low-energy spin-valley coupling in BLG QDs has remained experimentally unexplored. This is certainly partly due to

the high energy resolution required, as theoretical studies predict an intrinsic spin-orbit (SO) coupling in graphene and BLG of around $\Delta_{\text{SO}} \sim 24 \mu\text{eV}$ [12–16] and only recently, experiments have – partly indirectly – reported values in the range between 40 and 80 μeV [17, 18]. Moreover, our current knowledge with respect to a possible mixing of K and K' states is very limited. The latter is expressed by $\Delta_{\text{KK}'}$ and could allow to access helical states [19].

In this letter, we report on measurements of the excited state spectrum of a single-electron double quantum dot (DQD) in BLG providing information on Δ_{SO} as well as on $\Delta_{\text{KK}'}$. By tuning the DQD to a regime of low interdot tunnel coupling, we are able to resolve the interdot transitions with remarkably high energy resolution allowing to reconstruct the underlying single particle spectrum of both quantum dots. We find that the spin and valley degeneracy of the single particle spectrum is lifted by a Kane-Mele type SO gap [13] of $\Delta_{\text{SO}} \approx 65 \mu\text{eV}$, which separates the two Kramer's pairs – ($K'\uparrow, K'\downarrow$) and ($K\downarrow, K\uparrow$) – similar (but smaller in magnitude) to what has been observed in carbon nanotube QDs [20, 21]. The disorder-induced mixing of K and K' is found to be at least smaller than $\Delta_{\text{KK}'} < 20 \mu\text{eV}$. Fig. 1(b) depicts the first four BLG QD states composing the first electronic orbital (“shell”) as a function of the magnetic fields applied in-plane (B_{\parallel}) and out-of-plane (B_{\perp}) to the BLG sheet. At zero magnetic field, the four states are split into two Kramer's pairs, separated by Δ_{SO} . Applying an out-of-plane magnetic field linearly shifts the energy of the states according to the spin and valley Zeeman effects $E(B_{\perp}) = \frac{1}{2}(\pm g_s \pm g_v)\mu_B B_{\perp}$, where μ_B is the Bohr magneton and g_v is the valley g -factor, which quantifies the strength of the valley magnetic moment. Note that g_v strongly depends on the QD wave functions and thus on the size of the QD [11]. It is usually one order of magnitude larger than the spin g -factor, $g_s = 2$. As the valley magnetic moment is oriented perpendicular to the BLG plane, in-plane B -fields only couple to the electron spin. However, as the SO coupling acts as an effective out-of-plane magnetic field close to the K -points, the spin states are polarized perpendicular the BLG plane (see insets in Fig. 1(b)) [12]. Applying an in-plane magnetic field therefore shifts the states according to $E(B_{\parallel}) = \pm \frac{1}{2}\sqrt{\Delta_{\text{SO}}^2 + (g_s\mu_B B_{\parallel})^2}$ recovering the linear spin Zeeman effect for high B -fields.

The device consists of a BLG flake, which has been encapsulated between two flakes of hexagonal boron nitride (thickness of $\approx 25 \text{ nm}$) and placed on a graphite flake, acting as a back gate (BG), using a dry van-der-Waals stacking technique. Cr/Au split gates (SGs) are deposited on top, forming a $2 \mu\text{m}$ long and 130 nm wide channel. Two layers of metallic Cr/Au finger gates (FGs) with a width of 70 nm and a pitch of 150 nm are fabricated across the channel. Details on the fabrication process can be found in Ref. [6]. Fig. 2(a) shows a scanning electron micrograph of the gate structure, where the gates used as plunger gates are color coded.

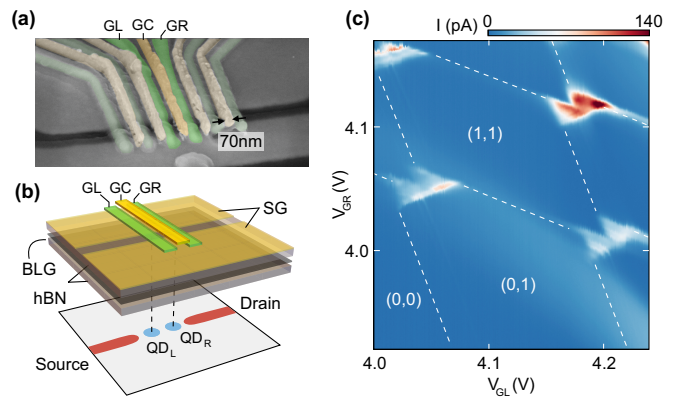


FIG. 2. (a) False-color scanning electron micrograph of the metallic gates. A pair of split gates defines the conducting channel, which can be modulated by voltages applied to the finger gates. The gates used in the following are color coded. (b) Schematic cross-section of the device. The upper part shows the metallic gates on top of the van-der-Waals heterostructure. The lower part color codes the charge carrier density within the channel and the two quantum dots (red: holes and blue: electrons). (c) Charge stability diagram showing the current through the double quantum dot as function of the potential applied to the two gate fingers, V_{GL} and V_{GR} . A constant bias voltage of $V_b = 1 \text{ mV}$ is applied and the central finger gate voltage is kept at $V_{\text{GC}} = -4 \text{ V}$.

Fig. 2(b) shows a schematic cross section through the heterostructure and the gate stack highlighting the formation of the QDs and source-drain regions by electrostatic soft-confinement. All measurements are performed in a helium dilution refrigerator at a base temperature of 10 mK , using standard DC measurement techniques.

QDs are created using three layers of top gates, following previous studies of gate-defined BLG QDs [5, 6, 9, 10, 22, 23]. A band gap is opened by applying an out-of-plane displacement field [24, 25] with the help of the SG ($V_{\text{SG}} = 1.73 \text{ V}$) and BG ($V_{\text{BG}} = -1.56 \text{ V}$), and the Fermi energy is tuned into the band gap. This leaves a narrow p-type conducting channel, connecting source and drain. A single electron DQD can be formed using adjacent FGs on the lower FG layer (GL and GR), locally overcompensating the BG voltage (see lower illustration in Fig. 2(b)) [6]. By applying $V_{\text{GC}} = -4 \text{ V}$ to the central FG between GL and GR, the interdot tunnel coupling is reduced in order to enhance the energy resolution of the bias spectroscopy measurements. Fig. 2(c) shows a charge stability diagram of the first four triple point pairs (see supp. material for more details).

Next, we focus on the the (0,1)-(1,0) charge transition, where each of the QDs is at most occupied by a single electron. Importantly, the combined tunneling rate is reduced to $\Gamma < 1 \text{ GHz}$ by GC on the upmost gate layer (see Fig. 2(a)). This reduces the tunnel broadening of the resonance lines and strongly suppresses transport if the states in the two QDs are off resonance. Figs. 3(a)-(c) show finite bias charge stability diagrams of the first triple point pair at out-of-plane magnetic fields of $B_{\perp} =$

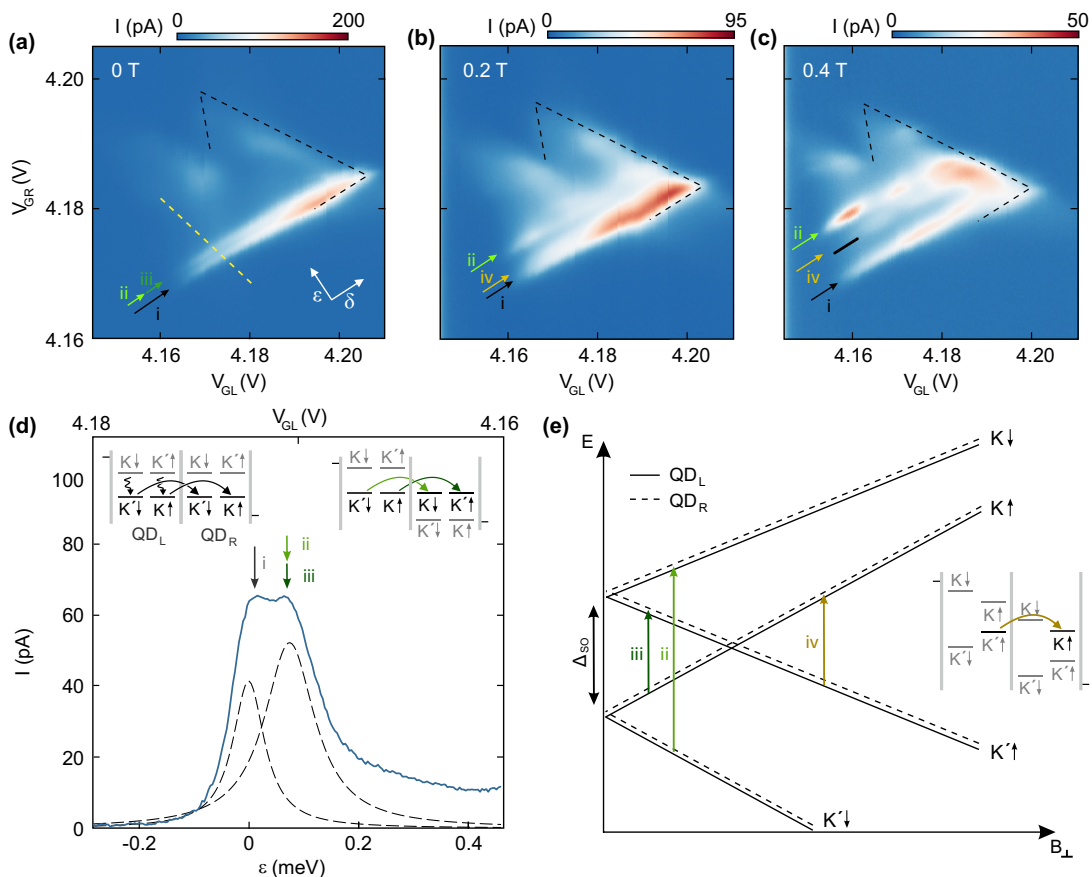


FIG. 3. (a)-(c) Charge stability diagrams of the first pair of triple points ((1,0)-(0,1) transition) measured at $V_b = 1$ mV and (a) $B_\perp = 0$ T, (b) $B_\perp = 0.2$ T, (c) $B_\perp = 0.4$ T. The white arrows in panel (a) indicate the orthogonal detuning axis ϵ and the DQD's common energy δ . At zero magnetic field two transition lines are visible (green and black arrows). (d) Cut along the yellow dashed line in the first triple point at $B = 0$ T. Two Lorentzian peaks are fit to the data to extract a splitting of $\Delta_{SO} = 68 \pm 7 \mu\text{eV}$. Inset: Schematic energy diagrams of a DQD in the finite bias regime for different interdot detuning energies ϵ , illustrating resonant transport through the ground state of each QD (transition (i); left inset) and resonant transport at $\epsilon = \Delta_{SO}$ (transitions (ii) and (iii); right inset). (e) Schematic of the single particle energy spectra of the first orbital of each QD as a function of B_\perp . The arrows (color coding as in panels (a)-(c)) indicate spin conserving transitions from single particle states in the left QD (solid lines) to single particle states in the right QD (dashed lines). The inset shows the transition (iv) at finite magnetic field.

0 – 0.4 T. In order to describe the configurations of the DQD, we introduce the orthogonal axes δ and ϵ , which describe how far the states in both QDs are tuned into the bias window (δ) and how large their energy detuning (ϵ) is, respectively [26]. At zero B -field, two resonances close to zero detuning (resonances (i) and (ii), (iii)) are visible, while the rest of the triple point shows only suppressed current. Increasing B_\perp shifts one of the resonances (ii) to higher detuning (compare green arrows in Figs. 3(a)-(c)). Eventually, a third resonance appears (iv), which does not extend as far on the δ -axis as the other transitions (see Fig. 3(c)).

The nature of these resonances can be explained in terms of transitions from single particle states in the left QD (QD_L) to single particle states in the right QD (QD_R). For the present interdot tunneling times (≈ 10 ns [27]), we assume that the electron spin is entirely conserved, while phonon assisted valley relaxation

may occur on these time scales, as well as during interdot tunneling [28]. Fig. 3(d) shows a line cut through the triple point in Fig. 3(a) along the yellow dashed line. The two transitions (black arrow and green arrows in Fig. 3(a)) result in two distinct peaks in the tunneling current. The first resonance, (i) occurs at $\epsilon = 0$, where every state in the left QD can tunnel into its equivalent state in the right QD, highlighted by the black arrow (see left schematic in Fig. 3(d)). The second resonance occurs at $\epsilon = \Delta_{SO} = 68 \pm 7 \mu\text{eV}$., where two processes are possible, both requiring valley flips, namely transition (ii): $(K'\downarrow)_L \Rightarrow (K\downarrow)_R$ and transition (iii): $(K\uparrow)_L \Rightarrow (K'\uparrow)_R$, highlighted by the two green arrows (see right schematic in Fig. 3(d)).

When applying an out-of-plane B -field, the energies of the single particle states shift according to their spin and valley Zeeman effect, as depicted on the right-hand side of Fig. 1(b). Consequently, the detuning energy necessary

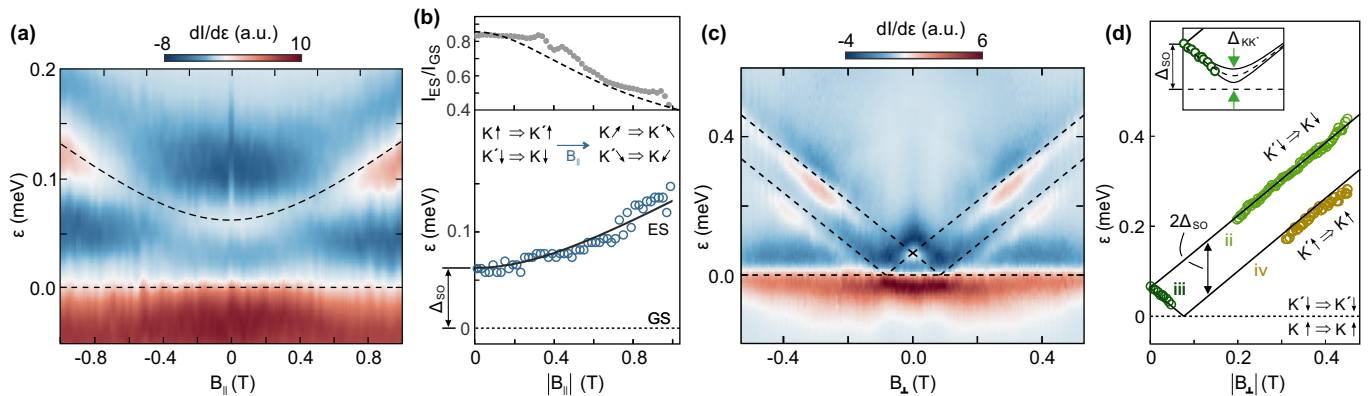


FIG. 4. **(a)** Magnetotransport measurements showing $dI/d\epsilon$ as function of detuning energy and in-plane B -field. The horizontal dashed line marks the ground state (GS) transition ($\epsilon = 0$) and the curved line marks the excited state (ES) transition. **(b)** The upper panel shows the ratio of the ES current with respect to the GS current. The dashed line describes the expected decay in amplitude of the ES due to the spins tilting in-plane and is given by $I_{ES}/I_{GS} \propto \sqrt{1 + (g_s \mu_B B_{||} / \Delta_{SO})^2}^{-1}$. The lower panel shows the extracted ES energy as function of $B_{||}$. This data is used for fitting (see text). **(c)** Similar data as in panel (a) but for out-of-plane B -field. The dashed lines mark all transitions described in Fig. 3(e). **(d)** Extracted transition energies as function of B_{\perp} highlighting the transitions (ii), (iii) and (iv) (see labels). The inset shows a low-energy close-up around the transition (iii) highlighting the presence of a finite $K - K'$ mixing. The dashed line corresponds to transition energies including a $\Delta_{KK'} = 20 \mu\text{eV}$. The solid lines below and above correspond to $\Delta_{KK'} = 10 \mu\text{eV}$ and $30 \mu\text{eV}$, respectively.

for the transition (ii) increases linearly with magnetic field, highlighted by the light green arrow in Fig. 3(e). The observed increase in detuning energy corresponds to a valley g -factor of $g_v \approx 15$. This observation validates the assumption that valley flips are allowed, since otherwise interdot transitions should not shift as function of B_{\perp} . The detuning required for transition (iii), decreases to zero, once the involved states are equal in energy, which is the case at $B_{\perp} \approx 0.18$ T (see Fig. 3(e)). At higher magnetic fields, the reversed process, transition (iv): $(K' \uparrow)_L \Rightarrow (K \uparrow)_R$ becomes possible, which also shifts with a valley g -factor of $g_v \approx 15$. This transition is marked by the orange arrow in Fig. 3(c) and offset to the transition (ii) by $\Delta\epsilon = 2\Delta_{SO}$, which becomes apparent from Fig. 3(e). Since transition (iv) originates from an excited state (ES) in the QDL, it only becomes accessible as soon as the ES enters the bias window. Therefore, the transition line (iv) has a shorter extend along the δ -axis, as it only sets in at finite δ , which is highlighted by the black line in Fig. 3(c). The observation of transition (iv) also justifies the assumption of spin conservation. If the spin lifetime would be shorter than the tunneling rate, $(K' \uparrow)_L$ would decay into $(K' \downarrow)_L$, blocking this process and the resonance would not be visible. Please note that the tunneling current corresponding to transitions (ii)-(iv) is energy (ϵ) and δ -dependent as resonant tunneling (in particular with the drain reservoir) leads to higher tunneling currents ((see Fig. 3(a)-(c)).

Fig. 4 shows the interdot transitions as function of in-plane (Fig. 4(a),(b)) and out-of-plane (Fig. 4(c),(d)) B -field highlighting the spin and valley texture of the low energy spectrum. In Fig. 4(a) we show the derivative of the tunneling current I with respect to ϵ as function of energy and $B_{||}$. Apart from the zero detuning

transition (horizontal dashed line), one additional feature is visible (curved dashed line), which corresponds to the transitions from the energetically lower Kramer's pair to the energetically higher Kramer's pair, namely $(K \uparrow)_L \Rightarrow (K' \uparrow)_R$ and $(K' \downarrow)_L \Rightarrow (K \downarrow)_R$, as highlighted by the schematic insets of Fig. 3(d). Increasing the in-plane B -field increases the energy difference between the Kramer's pairs due to the spin Zeeman effect and therefore the required detuning shifts according to $\epsilon = \sqrt{\Delta_{SO}^2 + (g_s \mu_B B)^2}$.

Fitting this equation with a fixed $g_s = 2$, which is in good agreement with earlier measurements [22], incl. electron spin resonance experiments [29], yields $\Delta_{SO} = 62 \pm 6 \mu\text{eV}$. This results in the dashed and solid line in Figs. 4(a),(b) showing good agreement with the experiment. Applying an in-plane magnetic field tilts the spin from an out-of-plane orientation induced by the SO coupling into the plane of the BLG (see insets in Fig. 4(b)). This effect continuously reduces the overlap between the spin states from different Kramer's pairs, e.g. the spin state from $K \uparrow$ is not perfectly parallel to $K' \uparrow$ anymore, until for large $B_{||}$ they will eventually be completely orthogonal. This effect becomes visible in the tunneling current of the ES transition, which decreases with increasing in-plane magnetic field. In the top panel of Fig. 4(b), we show the ratio between the current through the excited and the ground state ($\epsilon = 0$) as a function of $B_{||}$ highlighting this effect, which is in good agreement with what is expected from theory (see dashed line and figure caption).

Fig. 4(c) shows the derivative of the tunneling current with respect to ϵ , as function of energy and B_{\perp} . Here, according to Fig. 1(b) the transition spectra is significantly richer and all three transitions (ii), (iii) and (iv)

discussed in Fig. 3(e) can be observed (see dashed lines and labels in Fig. 4(d)). If we denote the valley g -factor in the left and right QD with $g_{v,L}$ and $g_{v,R}$, respectively, then we can express the different transition energies as a function of B_{\perp} by $\epsilon_{ii} = \Delta_{SO} + \frac{1}{2}(g_{v,R} + g_{v,L})\mu_B B_{\perp}$, $\epsilon_{iii} = \Delta_{SO} - \frac{1}{2}(g_{v,R} + g_{v,L})\mu_B B_{\perp}$, $\epsilon_{iv} = -\Delta_{SO} + \frac{1}{2}(g_{v,R} + g_{v,L})\mu_B B_{\perp}$. Here, the electron spin Zeeman effect has no influence on the transition energies, as transitions only occur between states of the same electron spin [30]. Taking Δ_{SO} from the analysis of the in-plane B -field data (Figs. 4(a),(b)) and choosing the valley g -factors to be $g_{v,L} = g_{v,R} = 15$ we find – without any additional parameter – good agreement with the experimental data (see dashed and solid lines in Figs. 4(c),(d)). The values of g_v are similar to those reported in previous studies of similar BLG QDs and compatible with theoretical calculations [6, 23]. Considering the same geometry of both QDs and the similar voltages applied to GL and GR, it is reasonable to assume that both QDs have very similar valley g -factors. Note that as soon as a transition requires negative detuning, it becomes Coulomb blocked, which is the reason why no transition is observed below $\epsilon = 0$. The lack of clear signatures of the transition (ii) at low B -field (see Fig. 4(c),(d)) can be explained by their reduced tunneling current compared to transition (iii) due to the stronger detuning of the $(K'\uparrow)_L$ ground state from the source chemical potential compared to $(K\uparrow)_L$, combined with strong resonant tunneling from source to the left QD.

By closely inspecting the transition (iii), especially close to the B -field regime where the $K\uparrow$ state is crossing the $K'\uparrow$ state (i.e. around $\epsilon = 0$ we can provide an estimate of the upper limit of a possible disorder-induced mixing of the K and K' states. The inset of Fig. 4(d)

shows a close up, where we included the expected transition energies for different values of $\Delta_{KK'}$. We do not observe any anticrossing and from this comparison we estimate that $\Delta_{KK'}$ is surely not exceeding a value of $20 \mu\text{eV}$ in our sample. Note that this upper limit is significantly smaller than for carbon nanotubes with values on the order of $100 \mu\text{eV}$ [20, 21].

In summary, we studied the low-energy excited state spectrum of a gate-defined single-electron quantum dot in bilayer graphene. We find a spin-valley coupling dominated by a Kane-Mele type SO coupling with $\Delta_{SO} \approx 65 \mu\text{eV}$, giving rise to two Kramer's pairs with either parallel or anti-parallel spin-valley orientation. The small value for $\Delta_{KK'} (< 20 \mu\text{eV})$ is not entirely unexpected for flat and disorder-free BLG, and raises the hope that the existing spin-valley coupling – without $K - K'$ mixing – will be helpful for a future qubit operation.

Acknowledgements The authors thank J. Klos for help with the SEM micrographs. This project has received funding from the European Union's Horizon 2020 research and innovation programme under grant agreement No. 881603 (Graphene Flagship) and from the European Research Council (ERC) under grant agreement No. 820254, the Deutsche Forschungsgemeinschaft (DFG, German Research Foundation) under Germany's Excellence Strategy - Cluster of Excellence Matter and Light for Quantum Computing (ML4Q) EXC 2004/1 - 390534769, through DFG (STA 1146/11-1), and by the Helmholtz Nano Facility [31]. Growth of hexagonal boron nitride crystals was supported by the Elemental Strategy Initiative conducted by the MEXT, Japan, Grant Number JPMXP0112101001, JSPS KAKENHI Grant Numbers JP20H00354 and the CREST(JPMJCR15F3), JST.

-
- [1] B. Trauzettel, D. V. Bulaev, D. Loss, and G. Burkard, Nat. Phys. **3**, 192 (2007).
 - [2] G. Y. Wu, N.-Y. Lue, and Y.-C. Chen, Phys. Rev. B **88**, 125422 (2013).
 - [3] E. McCann and M. Koshino, Rep. Prog. Phys. **76**, 056503 (2013).
 - [4] A. Knothe and V. Fal'ko, Phys. Rev. B **98**, 155435 (2018).
 - [5] M. Eich, R. Pisoni, A. Pally, H. Overweg, A. Kurzmann, Y. Lee, P. Rickhaus, K. Watanabe, T. Taniguchi, K. Ensslin, and T. Ihn, Nano Lett. **18**, 5042 (2018).
 - [6] L. Banszerus, A. Rothstein, T. Fabian, S. Möller, E. Icking, S. Trellenkamp, F. Lentz, D. Neumaier, K. Watanabe, T. Taniguchi, F. Libisch, C. Volk, and C. Stampfer, Nano Lett. **20**, 7709 (2020).
 - [7] Y. Lee, A. Knothe, H. Overweg, M. Eich, C. Gold, A. Kurzmann, V. Klasovika, T. Taniguchi, K. Watanabe, V. Fal'ko, T. Ihn, K. Ensslin, and P. Rickhaus, Phys. Rev. Lett. **124**, 126802 (2020).
 - [8] R. Garreis, A. Knothe, C. Tong, M. Eich, C. Gold, K. Watanabe, T. Taniguchi, V. Fal'ko, T. Ihn, K. Ensslin, and A. Kurzmann, arXiv (2020), 2011.07951.
 - [9] M. Eich, R. Pisoni, H. Overweg, A. Kurzmann, Y. Lee, P. Rickhaus, T. Ihn, K. Ensslin, F. Herman, M. Sigrist, K. Watanabe, and T. Taniguchi, Phys. Rev. X **8**, 031023 (2018).
 - [10] A. Kurzmann, M. Eich, H. Overweg, M. Mangold, F. Herman, P. Rickhaus, R. Pisoni, Y. Lee, R. Garreis, C. Tong, K. Watanabe, T. Taniguchi, K. Ensslin, and T. Ihn, Phys. Rev. Lett. **123**, 026803 (2019).
 - [11] A. Knothe and V. Fal'ko, Phys. Rev. B **101**, 235423 (2020).
 - [12] S. Konschuh, M. Gmitra, D. Kochan, and J. Fabian, Phys. Rev. B **85**, 115423 (2012).
 - [13] C. L. Kane and E. J. Mele, Phys. Rev. Lett. **95**, 226801 (2005).
 - [14] H. Min, J. E. Hill, N. A. Sinitsyn, B. R. Sahu, L. Kleinman, and A. H. MacDonald, Phys. Rev. B **74**, 165310 (2006).
 - [15] Y. Yao, F. Ye, X.-L. Qi, S.-C. Zhang, and Z. Fang, Phys. Rev. B **75**, 041401 (2007).

- [16] K. Zollner, M. Gmitra, and J. Fabian, *Phys. Rev. B* **99**, 125151 (2019).
- [17] L. Banszerus, B. Frohn, T. Fabian, S. Somanchi, A. Epping, M. Müller, D. Neumaier, K. Watanabe, T. Taniguchi, F. Libisch, B. Beschoten, F. Hassler, and C. Stampfer, *Phys. Rev. Lett.* **124**, 177701 (2020).
- [18] J. Sichau, M. Prada, T. Anlauf, T. J. Lyon, B. Bosnjak, L. Tiemann, and R. H. Blick, *Phys. Rev. Lett.* **122**, 046403 (2019).
- [19] J. Klinovaja, G. J. Ferreira, and D. Loss, *Phys. Rev. B* **86**, 235416 (2012).
- [20] F. Kuemmeth, S. Ilani, D. C. Ralph, and P. L. McEuen, *Nature* **452**, 448 (2008).
- [21] T. S. Jespersen, K. Grove-Rasmussen, J. Paaske, K. Muraki, T. Fujisawa, J. Nygård, and K. Flensberg, *Nat. Phys.* **7**, 348 (2011).
- [22] L. Banszerus, B. Frohn, A. Epping, D. Neumaier, K. Watanabe, T. Taniguchi, and C. Stampfer, *Nano Lett.* **18**, 4785 (2018).
- [23] C. Tong, R. Garreis, A. Knothe, M. Eich, A. Sacchi, K. Watanabe, T. Taniguchi, V. Fal'ko, T. Ihn, K. Ensslin, and A. Kurzmann, *Nano Lett.* **21**, 1068 (2021).
- [24] Y. Zhang, T.-T. Tang, C. Girit, Z. Hao, M. C. Martin, A. Zettl, M. F. Crommie, Y. R. Shen, and F. Wang, *Nature* **459**, 820 (2009).
- [25] J. B. Oostinga, H. B. Heersche, X. Liu, A. F. Morpurgo, and L. M. K. Vandersypen, *Nat. Mater.* **7**, 151 (2007).
- [26] In the single electron regime, the QD transitions (chemical potentials) are equivalent to the single particle energies.
- [27] We consider the combined tunneling rate, Γ_{comb} to be limited by the interdot tunneling rate, Γ_{m} : $I/e = \Gamma_{\text{comb}} \approx \Gamma_{\text{m}}$.
- [28] S. Reichardt and C. Stampfer, *Phys. Rev. B* **93**, 245423 (2016).
- [29] T. J. Lyon, J. Sichau, A. Dorn, A. Centeno, A. Pesquera, A. Zurutuza, and R. H. Blick, *Phys. Rev. Lett.* **119**, 066802 (2017).
- [30] If that was not the case, many more transitions would be possible, e.g. $(K'\downarrow)_{\text{L}} \Rightarrow (K'\uparrow)_{\text{R}}$, which would yield a line originating at $\epsilon = \Delta_{\text{SO}}$ with much flatter slope of $g_s = 2$.
- [31] W. Albrecht, J. Moers, and B. Hermanns, *Journal of Large-Scale Research Facilities* **3**, 112 (2017).

Supporting information: Spin-valley coupling in single-electron bilayer graphene quantum dots

L. Banszerus,^{1,2,*} S. Möller,^{1,2,*} C. Steiner,^{1,2} E. Icking,^{1,2} S. Trellenkamp,³
F. Lentz,³ K. Watanabe,⁴ T. Taniguchi,⁵ C. Volk,^{1,2} and C. Stampfer^{1,2,†}

¹*JARA-FIT and 2nd Institute of Physics,*

RWTH Aachen University, 52074 Aachen, Germany, EU

²*Peter Grünberg Institute (PGI-9), Forschungszentrum Jülich, 52425 Jülich, Germany, EU*

³*Helmholtz Nano Facility, Forschungszentrum Jülich, 52425 Jülich, Germany, EU*

⁴*Research Center for Functional Materials,*

National Institute for Materials Science,

1-1 Namiki, Tsukuba 305-0044, Japan

⁵*International Center for Materials Nanoarchitectonics,*

National Institute for Materials Science,

1-1 Namiki, Tsukuba 305-0044, Japan

(Dated: December 23, 2024)

* These two authors contributed equally.

† stampfer@physik.rwth-aachen.de

I. DETAILS ON SAMPLE DESIGN AND TUNING TOWARDS A SINGLE ELECTRON DQD

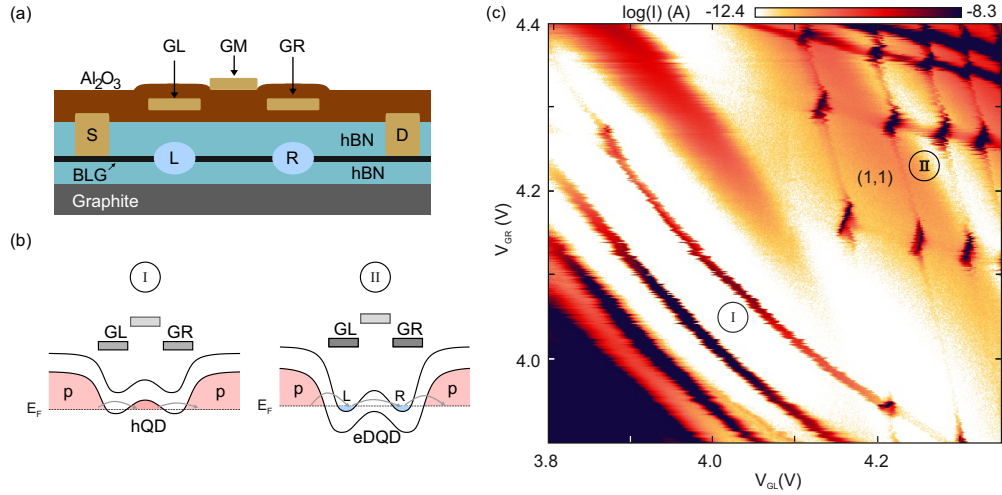


FIG. 1. (a) Schematic cross section through the device. BLG is encapsulated between two flakes of hBN and placed on a graphite gate. Two Cr/Au contacts (S and D) are evaporated onto the BLG. Two layers of Cr/Au FGs are used to form a DQD. Atomic layer deposited Al_2O_3 serves as a gate dielectric. (b) Band alignment of the single QD and DQD regimes. (c) Charge stability diagram of GL versus GR showing the that the triple point considered in the main text is indeed the (0,1)-(1,0) charge transition.